Chapter 5
Multiscale Homogenization Theory: An Analysis Tool for Revealing Mechanical Design Principles in Bone and Bone Replacement Materials

Christian Hellmich, Andreas Fritsch, and Luc Dormieux

Abstract Biomimetics deals with the application of nature-made "design solutions" to the realm of engineering. In the quest to understand mechanical implications of structural hierarchies found in biological materials, multiscale mechanics may hold the key to understand "building plans" inherent to entire material classes, here bone and bone replacement materials. Analyzing a multitude of biophysical hierarchical and biomechanical experiments through homogenization theories for upscaling stiffness and strength properties reveals the following design principles: The elementary component "collagen" induces, right at the nanolevel, the mechanical anisotropy of bone materials, which is amplified by fibrillar collagen-based structures at the 100-nm scale, and by pores in the micrometer-to-millimeter regime. Hydroxyapatite minerals are poorly organized, and provide stiffness and strength in a quasi-brittle manner. Water layers between hydroxyapatite crystals govern the inelastic behavior of the nanocomposite, unless the "collagen reinforcement" breaks. Bone replacement materials should mimic these "microstructural mechanics" features as closely as possible if an imitation of the natural form of bone is desired (Gebeshuber et al., Adv Mater Res 74:265–268, 2009).

Nomenclature

$\mathbb{a}_{rs}$	Fourth-order influence tensor
$\mathbb{A}_r$	Fourth-order strain concentration tensor of phase r
$\mathbb{c}_{\text{col}}$	Fourth-order stiffness tensor of molecular collagen
$c_{\text{col},ijkl}$	Component of fourth-order stiffness tensor of molecular collagen

C. Hellmich (✉)
Institute for Mechanics of Materials and Structures, Vienna University of Technology (TU Wien), Karlsplatz 13/202, 1040 Vienna, Austria
e-mail: christian.hellmich@tuwien.ac.at

P. Gruber et al. (eds.) *Biomimetics – Materials, Structures and Processes*, Biological and Medical Physics, Biomedical Engineering, DOI 10.1007/978-3-642-11934-7_5,

$\mathbb{c}_r$	Fourth-order stiffness tensor of phase r
$\mathbb{C}^{\text{hom}}$	Homogenized fourth-order stiffness tensor
$\mathbb{C}^0$	Fourth-order stiffness tensor of an infinite matrix surrounding an ellipsoidal inclusion
d	Characteristic length of the inhomogeneities within an RVE
$\boldsymbol{E}$	Second-order "macroscopic" strain tensor
$\boldsymbol{E}^{\text{p}}$	Second-order "macroscopic" plastic strain tensor
$\underline{e}_1, \underline{e}_2, \underline{e}_3$	Unit base vectors of Cartesian reference base frame
$\underline{e}_\vartheta, \underline{e}_\varphi, \underline{e}_r$	Unit base vectors of Cartesian local base frame of a single crystal of hydroxyapatite within extrafibrillar space
$\mathfrak{f}_r(\boldsymbol{\sigma}_r)$	Boundary r of elastic domain of phase r in space of microstresses
$\bar{f}_{\text{col}}$	Volume fraction of collagen within an RVE $\bar{V}_{\text{excel}}$
$\mathring{f}_{\text{col}}$	Volume fraction of molecular collagen within an RVE $\mathring{V}_{\text{wetcol}}$
$\bar{f}_{\text{ef}}$	Volume fraction of extrafibrillar space within an RVE $\bar{V}_{\text{excel}}$
$\tilde{f}_{\text{excel}}$	Volume fraction of extracellular bone matrix within an RVE $\tilde{V}_{\text{exvas}}$
f_{exvas}	Volume fraction of extravascular bone material within an RVE V_{cort}
$\bar{f}_{\text{fib}}$	Volume fraction of mineralized collagen fibril within an RVE $\bar{V}_{\text{excel}}$
$\bar{f}_{\text{HA}}$	Volume fraction of hydroxyapatite within an RVE $\bar{V}_{\text{excel}}$
$\check{f}_{\text{HA}}$	Volume fraction of hydroxyapatite within an RVE $\check{V}_{\text{fib}}$
$\check{f}_{\text{HA}}$	Volume fraction of hydroxyapatite within an RVE $\check{V}_{\text{ef}}$
$\check{f}_{\text{ic}}$	Volume fraction of intercrystalline space within an RVE $\check{V}_{\text{ef}}$
$\mathring{f}_{\text{im}}$	Volume fraction of intermolecular water within an RVE $\mathring{V}_{\text{wetcol}}$
$\tilde{f}_{\text{lac}}$	Volume fraction of lacunae within an RVE $\tilde{V}_{\text{exvas}}$
f_r	Volume fraction of phase r
f_{vas}	Volume fraction of Haversian canals within an RVE V_{cort}
$\check{f}_{\text{wetcol}}$	Volume fraction of wet collagen within an RVE $\check{V}_{\text{fib}}$
HA	Hydroxyapatite
$\mathbb{I}$	Fourth-order identity tensor
k_{HA}	Bulk modulus of hydroxyapatite
$k_{\text{H}_2\text{O}}$	Bulk modulus of water
$\mathcal{L}$	Characteristic lengths of geometry or loading of a structure built up by the material defined on the RVE
ℓ	Characteristic length of an RVE
ℓ_{cort}	Characteristic length of an RVE V_{cort} of cortical bone material
ℓ_{ef}	Characteristic length of an RVE $\check{V}_{\text{ef}}$ of extrafibrillar space
ℓ_{excel}	Characteristic length of an RVE $\bar{V}_{\text{excel}}$ of extracellular bone matrix
ℓ_{exvas}	Characteristic length of an RVE $\tilde{V}_{\text{exvas}}$ of extravascular bone material
ℓ_{fib}	Characteristic length of an RVE $\check{V}_{\text{fib}}$ of mineralized collagen fibril
ℓ_{wetcol}	Characteristic length of an RVE $\mathring{V}_{\text{col}}$ of wet collagen

$\underline{N}$	Orientation vector aligned with longitudinal axis of hydroxyapatite needle
n_r	Number of material phases within an RVE
$\underline{n}$	Orientation vector perpendicular to $\underline{N}$
RVE	Representative volume element
r	Index denoting a material phase
$\mathbb{P}_r^0$	Fourth-order Hill tensor characterizing the interaction between the phase r and the matrix $\mathbb{C}^0$
$\mathring{V}_{\text{col}}$	Volume of molecular collagen within an RVE $\mathring{V}_{\text{wetcol}}$
V_{cort}	Volume of RVE "cortical bone material"
$\breve{V}_{\text{ef}}$	Volume of RVE "extrafibrillar space"
$\bar{V}_{\text{ef}}$	Volume of extrafibrillar space within an RVE $\bar{V}_{\text{excel}}$
$\bar{V}_{\text{excel}}$	Volume of RVE "extracellular bone matrix"
$\tilde{V}_{\text{excel}}$	Volume of extracellular bone matrix within an RVE $\tilde{V}_{\text{exvas}}$
$\tilde{V}_{\text{exvas}}$	Volume of RVE "extravascular bone material"
V_{exvas}	Volume of extravascular bone material within an RVE V_{cort}
$\breve{V}_{\text{fib}}$	Volume of RVE "mineralized collagen fibril"
$\bar{V}_{\text{fib}}$	Volume of mineralized collagen fibril within an RVE $\bar{V}_{\text{excel}}$
$\breve{V}_{\text{HA}}$	Volume of hydroxyapatite within an RVE $\breve{V}_{\text{fib}}$
$\breve{V}_{\text{HA}}$	Volume of hydroxyapatite within an RVE $\breve{V}_{\text{ef}}$
$\breve{V}_{\text{ic}}$	Volume of intercrystalline space within an RVE $\breve{V}_{\text{ef}}$
$\mathring{V}_{\text{im}}$	Volume of intermolecular water within an RVE $\mathring{V}_{\text{wetcol}}$
$\tilde{V}_{\text{lac}}$	Volume of lacunae within an RVE $\tilde{V}_{\text{exvas}}$
V_{vas}	Volume of Haversian canals within an RVE V_{cort}
$\mathring{V}_{\text{wetcol}}$	Volume of RVE "wet collagen"
$\breve{V}_{\text{wetcol}}$	Volume of wet collagen within an RVE $\breve{V}_{\text{fib}}$
$\boldsymbol{\varepsilon}_r$	Second-order "microscopic" strain tensor field within phase r
$\dot{\boldsymbol{\varepsilon}}_r$	Incremental "microscopic" second-order strain tensor field within phase r
$\boldsymbol{\varepsilon}_r^{\text{p}}$	Second-order "microscopic" plastic strain tensor field within phase r
$\dot{\lambda}_r$	Incremental plastic multiplier
ϑ	Latitudinal coordinate of spherical coordinate system
θ	Integration variable, $\theta = 0 \ldots \pi$
μ_{HA}	Shear modulus of hydroxyapatite
$\mu_{\text{H}_2\text{O}}$	Shear modulus of water
$\boldsymbol{\sigma}_{\text{col}}$	Second-order stress tensor field within molecular collagen
$\sigma_{\text{col}}^{\text{ult}}$	Uniaxial tensile or compressive strength of molecular collagen
$\sigma_{\text{HA}}^{\text{NN}}$	Normal component of stress tensor $\boldsymbol{\sigma}_{\text{HA}\vartheta\varphi}$ in needle direction
σ_{HA}^{Nn}	Shear component of stress tensor $\boldsymbol{\sigma}_{\text{HA}\vartheta\varphi}$ in planes orthogonal to the needle direction
$\sigma_{\text{HA}}^{\text{ult,s}}$	Uniaxial shear strength of pure HA

$\sigma_{HA}^{ult,t}$	Uniaxial tensile strength of pure HA
$\boldsymbol{\sigma}_r$	Second-order stress tensor field within phase r
$\boldsymbol{\Sigma}$	Second-order "macroscopic" stress tensor
φ	Longitudinal coordinate of spherical coordinate system
ψ	Longitudinal coordinate of vector $\underline{n}$
$\cdot$	First-order tensor contraction
:	Second-order tensor contraction

5.1 Introduction

Biomimetics deals with the application of nature-made "design solutions" to the realm of engineering. In this context, large efforts have aimed at imitating biological materials with interesting mechanical properties. However, biological materials are hierarchically organized and very complex, and frequently, the way they work is not easily comprehensible [1]. Hence, successful biomimetics solutions require a deep understanding of "universal" functioning principles of biological materials. It now appears that multiscale mechanics may hold the key to such an understanding of "building plans" inherent to entire material classes.

For relating the vision of hierarchical organization of materials to effective mechanical properties, we rely on continuum micromechanics, which is a well-established tool for structure–property investigations.

Based on various physical–chemical and mechanical experiments, our focus is the development of multiscale mechanical models, which mathematically and computationally quantify how the basic building blocks of biological materials (such as hydroxyapatite minerals, collagen, and water in all bones found throughout the vertebrate kingdom) govern the materials' mechanical properties at different length scales, from a few nanometers up to the macroscopic level. Thereby, multiscale homogenization theory allows us, at each scale, to identify material representations which are as simple as possible, but as complex as necessary for reliable computational predictions of key material properties, such as poroelasticity, creep, and strength. This can be seen as "reverse" biomimetics engineering: (civil) engineering methods are used to understand biological systems, as described in more detail in Sect. 5.2.

This chapter is mainly devoted to the highly fascinating, hierarchically organized material class "bone" (see Sect. 5.3), and to the "universal" elementary building blocks inherent to this material class (Sect. 5.4). A multiscale micromechanics representation (Sect. 5.5) has opened, for the first time, a profound theoretical understanding of bone mechanics, which is consistent with virtually all major experimental observations, given in more detail in Sect. 5.6. One of our key findings is that bone's mechanical properties are governed by porous polycrystals which the minerals build up as structural complement to the collagen fibrils found in all connective tissues (also in tendon, cartilage, skin). These polycrystals are central

not only to the magnitude of elastic anisotropy of bone materials, but also to their tensile-to-compressive strength ratio resulting from universal failure characteristics of differently oriented submicron-sized mineral platelets (Sect. 5.7). Implications of these findings for bone biomaterial design conclude the chapter.

5.2 Fundamentals of Continuum Micromechanics

5.2.1 Representative Volume Element

In continuum micromechanics [2–6], a material is understood as a macrohomogeneous, but microheterogeneous body filling a representative volume element (RVE) with characteristic length $\ell, \ell \gg d$, d standing for the characteristic length of inhomogeneities within the RVE (see Fig. 5.1), and $\ell \ll \mathcal{L}$, $\mathcal{L}$ standing for the characteristic lengths of geometry or loading of a structure built up by the material defined on the RVE.

In general, the microstructure within one RVE is so complicated that it cannot be described in complete detail. Therefore, quasi-homogeneous subdomains with known physical quantities (such as volume fractions or elastoplastic properties) are reasonably chosen. They are called material phases. The "homogenized" mechanical behavior of the overall material, i.e., the relation between homogeneous deformations acting on the boundary of the RVE and resulting (average) stresses, including the ultimate stresses sustainable by the RVE, can then be estimated from the mechanical behavior of the aforementioned homogeneous phases (representing the inhomogeneities within the RVE), their dosages within the RVE, their

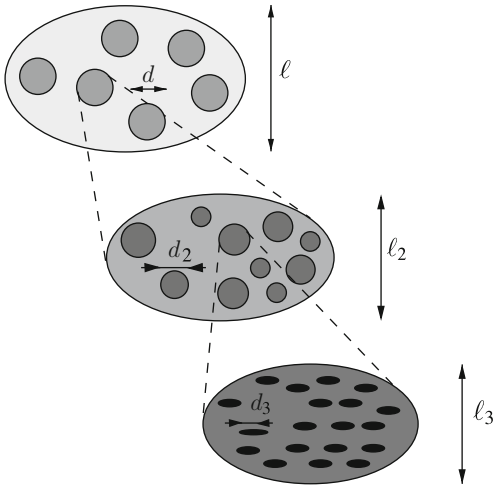

Fig. 5.1 Multistep homogenization: Properties of phases (with characteristic lengths of d and d_2, respectively) inside RVEs with characteristic lengths of ℓ or ℓ_2, respectively, are determined from homogenization over smaller RVEs with characteristic lengths of $\ell_2 \leq d$ and $\ell_3 \leq d_2$, respectively

characteristic shapes, and their interactions. If a single phase exhibits a heterogeneous microstructure itself, its mechanical behavior can be estimated by introduction of an RVE within this phase, with dimensions $\ell_2 \leq d$, comprising again smaller phases with characteristic length $d_2 \ll \ell_2$, and so on, leading to a multistep homogenization scheme (see Fig. 5.1).

5.2.2 *Upscaling of Elasto-Brittle and Elastoplastic Material Properties*

We consider an RVE consisting of n_r material phases, $r = 1, \ldots, n_r$, exhibiting elastoplastic or elasto-brittle material behavior. In case of ideal associated elastoplasticity, the RVE follows the constitutive laws:

$$\boldsymbol{\sigma}_r = \mathbb{c}_r : (\boldsymbol{\varepsilon}_r - \varepsilon_r^{\mathrm{p}}), \tag{5.1}$$

$$\dot{\boldsymbol{\varepsilon}}_r^{\mathrm{p}} = \dot{\lambda}_r \frac{\partial \mathfrak{f}_r}{\partial \boldsymbol{\sigma}_r}, \quad \dot{\lambda}_r \mathfrak{f}_r(\boldsymbol{\sigma}_r) = 0, \quad \dot{\lambda}_r \geq 0, \quad \mathfrak{f}_r(\boldsymbol{\sigma}_r) \leq 0. \tag{5.2}$$

In (5.2), $\boldsymbol{\sigma}_r$ and $\boldsymbol{\varepsilon}_r$ are the stress and (linearized) strain tensors averaged over phase r with elasticity tensor $\mathbb{c}_r$; $\boldsymbol{\varepsilon}_r^{\mathrm{p}}$ are the average plastic strains in phase r, λ_r is the plastic multiplier of phase r, and $\mathfrak{f}_r(\boldsymbol{\sigma}_r)$ is the yield function describing the (ideally) plastic characteristics of phase r.

In case of brittleness, the RVE follows the constitutive laws:

$$\boldsymbol{\sigma}_r = \mathbb{c}_r : \boldsymbol{\varepsilon}_r \quad (\boldsymbol{\varepsilon}_r^{\mathrm{p}} = \mathbf{0}) \quad \text{if} \quad \mathfrak{f}_r(\boldsymbol{\sigma}_r) < 0, \tag{5.3}$$

$\mathfrak{f}_r(\boldsymbol{\sigma}_r)$ now being a failure function defining stress states $\boldsymbol{\sigma}_r$ related to brittle failure.

The RVE is subjected to Hashin boundary conditions, i.e., to "homogeneous" ("macroscopic") strains $\boldsymbol{E}$ at its boundary, so that the kinematically compatible phase strains $\boldsymbol{\varepsilon}_r$ inside the RVE fulfill the average condition

$$\boldsymbol{E} = \sum_r f_r \boldsymbol{\varepsilon}_r \tag{5.4}$$

with f_r as the volume fraction of phase r. In a similar way, the equilibrated phase stresses $\boldsymbol{\sigma}_r$ fulfill the stress average condition

$$\boldsymbol{\Sigma} = \sum_r f_r \boldsymbol{\sigma}_r \tag{5.5}$$

with $\boldsymbol{\Sigma}$ as the "macroscopic" stresses.

The superposition principle (following from linear elasticity and linearized strain) implies that the phase strains $\boldsymbol{\varepsilon}_r$ are linearly related to both the macroscopic

strains $\boldsymbol{E}$ and the free strains $\boldsymbol{\varepsilon}_r^{\mathrm{p}}$ (which can be considered as independent loading parameters),

$$\boldsymbol{\varepsilon}_r = \mathbb{A}_r : \boldsymbol{E} + \sum_s \mathbb{a}_{rs} : \boldsymbol{\varepsilon}_s^{\mathrm{p}} \tag{5.6}$$

with $\mathbb{A}_r$ as the fourth-order concentration tensor [7], and $\mathbb{a}_{rs}$ as the fourth-order influence tensors [8]. The latter quantify the phase strains $\boldsymbol{\varepsilon}_r$ resulting from plastic strains $\boldsymbol{\varepsilon}_s^{\mathrm{p}}$, while the overall RVE is free from deformation, $\boldsymbol{E} = \boldsymbol{0}$.

In the absence of plastic strains [$\mathfrak{f}_r < 0$, $\boldsymbol{\varepsilon}_r^{\mathrm{p}} = \boldsymbol{0}$ in (5.1)–(5.2)], the RVE behaves fully elastically, so that (5.6), (5.5), (5.4), and (5.1) yield a macroscopic elastic law of the form:

$$\boldsymbol{\Sigma} = \mathbb{C}^{\mathrm{hom}} : \boldsymbol{E} \quad \text{with} \quad \mathbb{C}^{\mathrm{hom}} = \sum_r f_r \mathbb{c}_r : \mathbb{A}_r, \tag{5.7}$$

as the homogenized elastic stiffness tensor characterizing the material within the RVE. In case of nonzero "free" plastic strains $\boldsymbol{\varepsilon}_r^{\mathrm{p}}$, (5.7) can be extended to the form:

$$\boldsymbol{\Sigma} = \mathbb{C}^{\mathrm{hom}} : (\boldsymbol{E} - \boldsymbol{E}^{\mathrm{p}}), \tag{5.8}$$

(5.8), together with (5.1), (5.5)–(5.7), gives access to the macroscopic plastic strains $\boldsymbol{E}^{\mathrm{p}}$, reading as:

$$\boldsymbol{E}^{\mathrm{p}} = -\left[\sum_r f_r \mathbb{c}_r : \mathbb{A}_r\right]^{-1} : \left\{\sum_r f_r \mathbb{c}_r : \left[(\mathbb{A}_r : \boldsymbol{E} + \sum_s \mathbb{a}_{rs} : \boldsymbol{\varepsilon}_s^{\mathrm{p}}) - \boldsymbol{\varepsilon}_r^{\mathrm{p}}\right]\right\} + \boldsymbol{E}. \tag{5.9}$$

Matrix-inclusion problems [9, 10] allow for estimating concentration tensors $\mathbb{A}_r$ and influence tensors $\mathbb{a}_{rs}$ [11], so that the estimate for the homogenized stiffness (5.7) can be written as [5]:

$$\mathbb{C}^{\mathrm{hom}} = \sum_r f_r \mathbb{c}_r : \left[\mathbb{I} + \mathbb{P}_r^0 : (\mathbb{c}_r - \mathbb{C}^0)\right]^{-1} : \left\{\sum_s f_s \left[\mathbb{I} + \mathbb{P}_s^0 : (\mathbb{c}_s - \mathbb{C}^0)\right]^{-1}\right\}^{-1}, \tag{5.10}$$

where $\mathbb{I}$ is the fourth-order unity tensor, and the fourth-order Hill tensor $\mathbb{P}_r^0$ accounts for the characteristic shape of phase r in a matrix with stiffness $\mathbb{C}^0$. The two sums are taken over all phases of the heterogeneous material in the RVE. Choice of this stiffness describes the interactions between the phases: For $\mathbb{C}^0$ coinciding with one of the phase stiffnesses (Mori–Tanaka scheme [12, 13]), a composite material is represented (contiguous matrix with inclusions); for $\mathbb{C}^0 = \mathbb{C}^{hom}$ (self-consistent scheme [2, 14]), a dispersed arrangement of the phases is considered (typical for polycrystals).

5.3 Bone's Hierarchical Organization

Bone materials are characterized by an astonishing variability and diversity. Still, because of "architectural constraints" due to once chosen material constituents and their physical interaction, the fundamental hierarchical organization or basic building plans of bone materials remain largely unchanged during biological evolution. These building plans are expressed by typical morphological features which can be discerned across all bone materials. We here distinguish six levels of hierarchical organization in the line of Katz et al. [15], which have been quite generally accepted in the scientific community:

- At an observation scale of several 10 nm, the so-called elementary components of mineralized tissues can be distinguished. Long cylindrically shaped collagen molecules with a diameter of about 1.2 nm and a length of about 300 nm [16] are self-assembled in staggered organizational schemes with characteristic diameters of 50–500 nm [17–24], and attached to each other at their ends by crosslinks. These cross-linked collagen molecules build up, together with the water-filled intermolecular space, the scale of wet collagen (Fig. 5.2a).

  Needle or plate-shaped mineral crystals, consisting of impure hydroxyapatite (HA; $Ca_{10}[PO_4]_6[OH]_2$) with typical 1–5 nm thickness, and 25–50 nm length [22], are penetrated by the water-filled intercrystalline space (Fig. 5.2c).
- Wet collagen is penetrated by intrafibrillar crystals, forming a collagen–HA network, called fibril (Fig. 5.2b), at an observation scale of about 10 nm.
- The extrafibrillar crystals form aggregates and build up, together with the intercrystalline space, a porous HA polycrystal called extrafibrillar space (Fig. 5.2c), at an observation scale of about 300 nm.
- At an observation scale of several micrometers, the ultrastructure comprises the fibrils (light areas in Fig. 5.2d) and the extrafibrillar space (dark areas in Fig. 5.2d).
- At an observation scale of 100–200 μm, the extravascular bone matrix comprises the ultrastructure and osteocyte-filled cavities called lacunae (Fig. 5.2e).
- At an observation scale of several 100 μm to several millimeters, the microstructure comprises the extravascular bone matrix and the vascular space (Haversian canals) (Fig. 5.2f).

5.4 Elastic and Strength Properties of the Elementary Components of Bone: Hydroxyapatite, Collagen, Water

As regards hydroxyapatite, tests with an ultrasonic interferometer coupled with a solid media pressure apparatus [28, 29] reveal isotropic elastic properties, which are in perfect agreement with recent ab initio calculations of elastic constants of

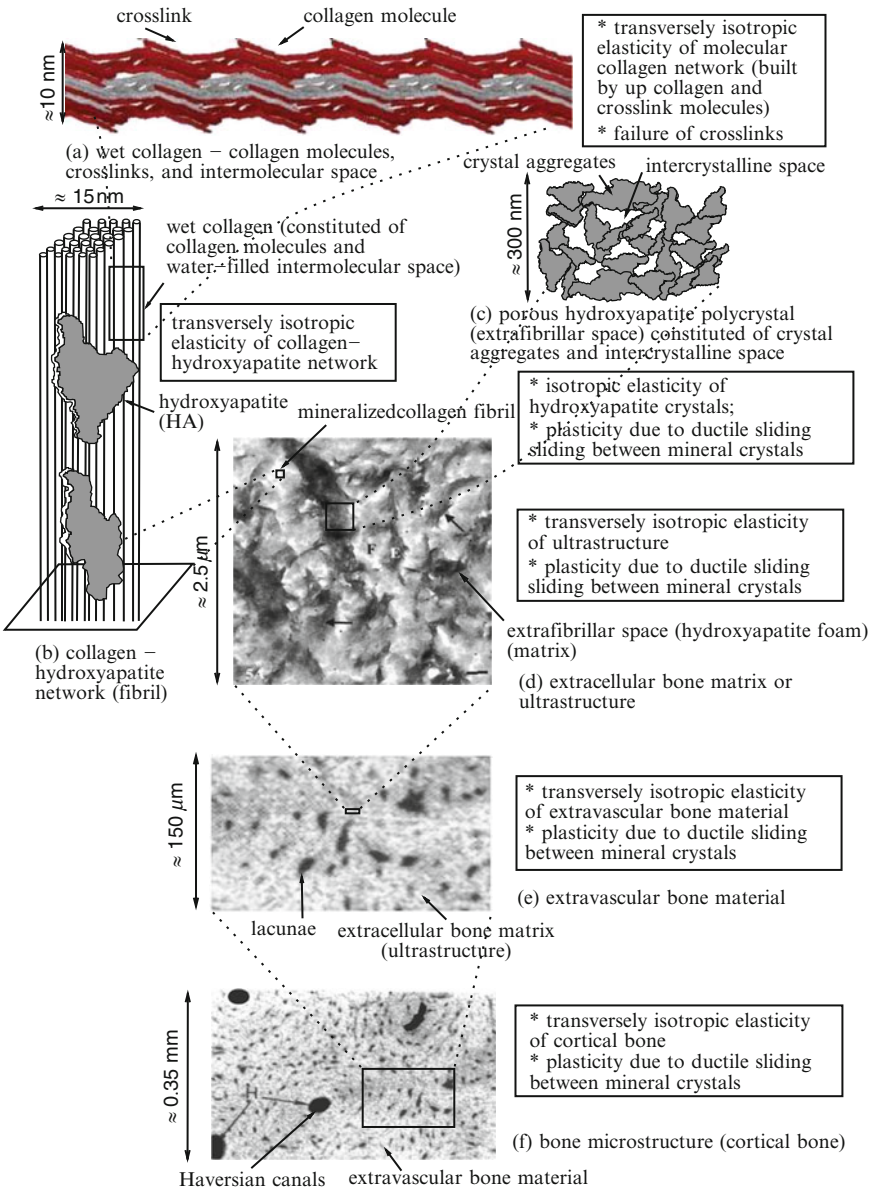

Fig. 5.2 Multiscale view of bone structure, with key physical effects considered in micromechanics representation of Fig. 5.4: (**a**) wet collagen; reproduced from [25], Copyright National Academy of Sciences, USA; (**b**) mineralized collagen fibril; schematic sketch after [26]; (**c**) extrafibrillar porous polycrystal; (**d**) extracellular bone matrix; reproduced with kind permission from Springer Science+Business Media: [24], Fig. 5; (**e**) extravascular bone matrix [zoomed out of image (**f**)]; (**f**) cortical bone; reprinted from [27], with permission from American Institute of Physics, ©1979

Table 5.1 "Universal" (tissue and location-independent) elasticity and strength values of elementary constituents of bone

Material phase	Elasticity (GPa)	Strength (MPa)
	k... bulk modulus	
	μ... shear modulus	$\sigma^{\mathrm{ult,t}}$... uniaxial (tensile) strength
	c_{ijkl}... tensor components, base frame according to Fig. 5.4	$\sigma^{\mathrm{ult,s}}$... shear strength
Hydroxyapatite (experimental source)	$k_{\mathrm{HA}} = 82.6$ [28]	$\sigma^{\mathrm{ult,t}}_{\mathrm{HA}} = 52.2$ [32, 33]
	$\mu_{\mathrm{HA}} = 44.9$ [28]	$\sigma^{\mathrm{ult,s}}_{\mathrm{HA}} = 80.3$ [32, 33]
Water containing noncollagenous organics or osteocytes	$k_{\mathrm{H_2O}} = 2.3$ [35]	
	$\mu_{\mathrm{H_2O}} = 0$	
Collagen (experimental source)	$c_{\mathrm{col},3333} = 17.9$	
	$c_{\mathrm{col},1111} = 11.7$	
	$c_{\mathrm{col},1133} = 7.1$	
	$c_{\mathrm{col},1122} = 5.1$	
	$c_{\mathrm{col},1313} = 3.3$ [17]	$\sigma^{\mathrm{ult}}_{\mathrm{col}} = 144.7$ [36, 37]

ceramic crystals [30, 31] (Table 5.1); and quasi-static mechanical tests in uniaxial tension and compression on fairly dense samples of artificial hydroxyapatite biomaterials [32, 33] give access to the uniaxial tensile and shear strength of pure hydroxyapatite (Table 5.1). The latter is probably governed by detachment of one nonspherical nano- or microcrystal of hydroxyapatite from its neighbors [34]. This is mathematically expressed through [11]:

$$\psi = 0, \ldots, 2\pi:$$
$$\mathrm{f}_{\mathrm{HA}\varphi\vartheta}(\boldsymbol{\sigma}_{\mathrm{HA}\varphi\vartheta}) = \frac{\sigma^{\mathrm{ult,t}}_{\mathrm{HA}}}{\sigma^{\mathrm{ult,s}}_{\mathrm{HA}}} \max_{\psi} |\sigma^{Nn}_{\mathrm{HA}}| + \sigma^{NN}_{\mathrm{HA}} - \sigma^{ult,t}_{HA} = 0 \tag{5.11}$$

with spherical coordinates φ and ϑ defining the crystal needle orientation vector $\underline{N} = \underline{e}_r$ in the reference frame $(\underline{e}_1, \underline{e}_2, \underline{e}_3)$, and with ψ defining the orientation of vector $\underline{n}$ related to shear stresses (see Fig. 5.3), with $\sigma^{\mathrm{ult,t}}_{\mathrm{HA}}$ as the uniaxial tensile strength and $\sigma^{\mathrm{ult,s}}_{\mathrm{HA}}$ as the shear strength of pure hydroxyapatite; and with $\sigma^{Nn}_{\mathrm{HA}} = \underline{N} \cdot \boldsymbol{\sigma}_{\mathrm{HA}\varphi\vartheta} \cdot \underline{n}$ and $\sigma^{NN}_{\mathrm{HA}} = \underline{N} \cdot \boldsymbol{\sigma}_{\mathrm{HA}\varphi\vartheta} \cdot \underline{N}$ as the normal and shear stress components related to a surface with normal $\underline{N}(\varphi, \vartheta)$.

As regards (molecular) collagen, its (transversely isotropic) elastic properties are well accessible through those of dry rat tail tendon, a tissue consisting almost exclusively of collagen (i.e., the intermolecular porous space, which is increasing with the water content of "wet collagen," is minimal for "dry collagen" [16, 37]). Corresponding components of the elasticity tensor of (molecular) collagen (see Table 5.1), derived from Brillouin light scattering tests [17], are in perfect agreement with Young's modulus of a collagen I monomer, when measured through an optical

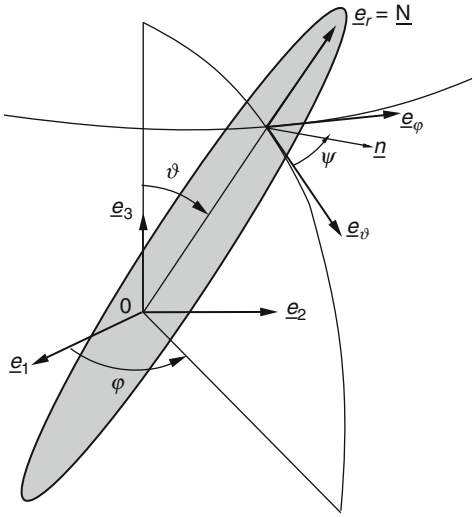

Fig. 5.3 Cylindrical (needle-like) HA inclusion oriented along vector $\underline{N}$ and inclined by angles ϑ and φ with respect to the reference frame $(\underline{e}_1, \underline{e}_2, \underline{e}_3)$; local base frame $(\underline{e}_r, \underline{e}_\vartheta, \underline{e}_\varphi)$ is attached to the needle

tweezer-interferometer system [38]. Strength tests, also on rat tail tendon [36], reveal the crosslink-failure-induced quasi-brittle strength of collagen [39], when related to the molecular collagen portion of the tissue [11] (see Table 5.1). The latter is mathematically expressed through [11]:

$$\mathrm{f}_{\mathrm{col}}(\boldsymbol{\sigma}_{\mathrm{col}}) = |\underline{e}_3 \cdot \boldsymbol{\sigma}_{\mathrm{col}} \cdot \underline{e}_3| - \sigma_{\mathrm{col}}^{\mathrm{ult}} \leq 0, \tag{5.12}$$

where the direction three coincides with the principal orientation direction of collagen and where $\sigma_{\mathrm{col}}^{\mathrm{ult}}$ is the uniaxial (tensile and compressive) strength of molecular collagen (see Fig. 5.4).

We assign the ultrasonics-derived bulk modulus of water [35] (and no strength value) to phases comprising water with mechanically insignificant noncollagenous organic matter (Table 5.1).

5.5 Multiscale Micromechanical Representation of Bone

Across the hierarchical organization of cortical bone material, the following "universal" microstructural patterns are considered in the framework of a multistep homogenization scheme (Fig. 5.4, see [11,40,41] for details): The first homogenization step refers to an observation scale of several nanometers, where cross-linked collagen molecules form a (linear elastic-perfectly brittle) contiguous matrix, which is "perforated" by intermolecular, water-filled spaces. A Mori–Tanaka scheme relates the stiffnesses and volume fractions of molecular collagen and intermolecular

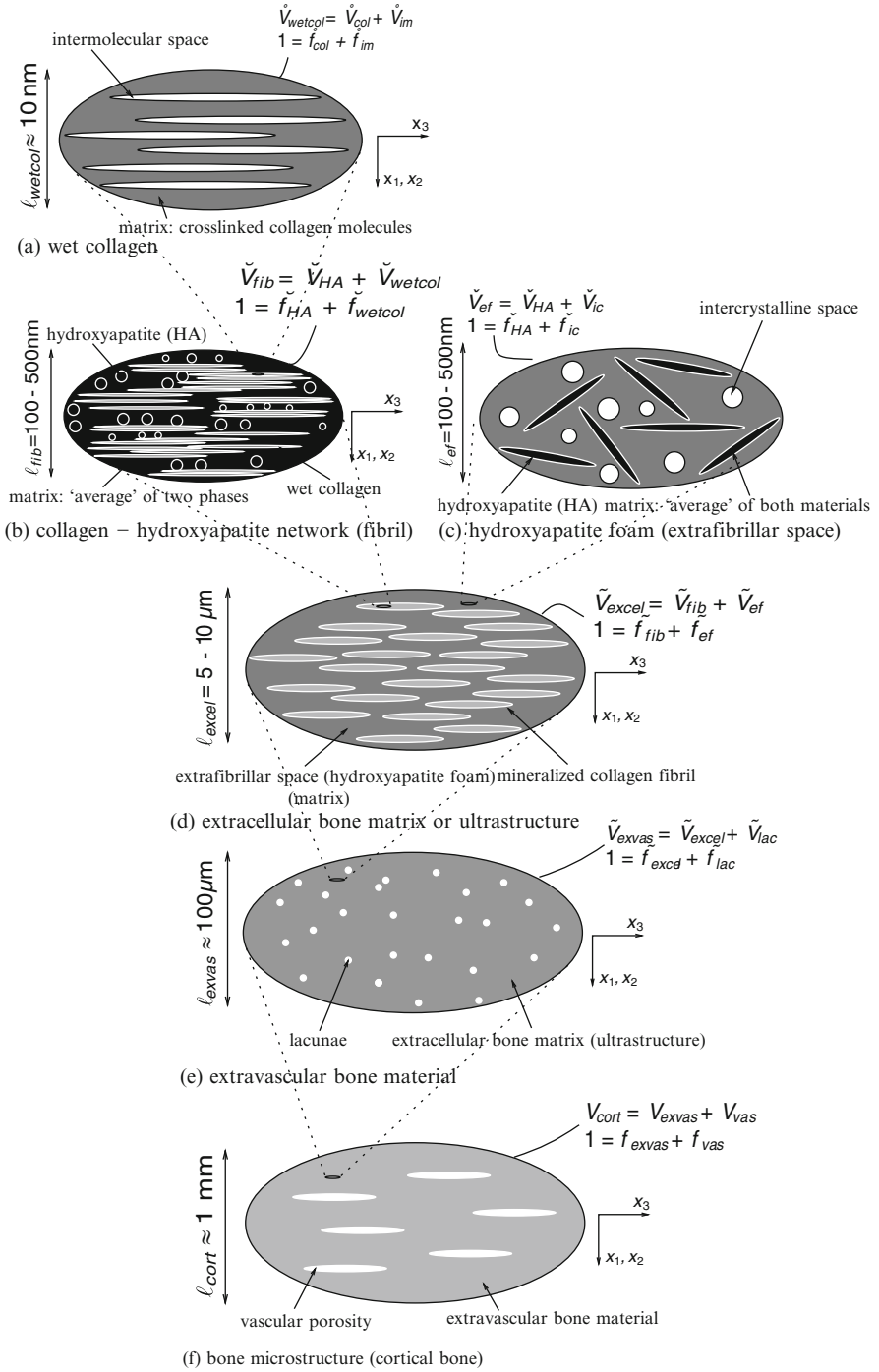

Fig. 5.4 Micromechanical representation of bone material by means of a six-step homogenization procedure. Reproduced from [11]

space to the homogenized elasticity tensor of wet collagen [specification of (5.10) for RVE of Fig. 5.4a]. The second homogenization step refers to an observation scale of several hundreds of nanometers, where wet collagen and mineral crystal agglomerations penetrate each other, building up the mineralized collagen fibril. A self-consistent scheme relates the stiffnesses and volume fractions of wet collagen and (intrafibrillar) hydroxyapatite crystal agglomerations to the homogenized elasticity tensor of the fibril [specification of (5.10) for RVE of Fig. 5.4b]. The third homogenization step also refers to an observation scale of several hundreds of nanometers, where (extrafibrillar) hydroxyapatite crystal agglomerations and intercrystalline space build up a porous polycrystal (extrafibrillar space). A self-consistent scheme relates the stiffnesses and volume fractions of hydroxyapatite crystals and intercrystalline space to the homogenized elasticity tensor of the porous hydroxyapatite crystal [specification of (5.10) for RVE of Fig. 5.4c]. The fourth homogenization step refers to an observation scale of some micrometers, where mineralized fibrils are embedded as inclusions into the extrafibrillar mineral foam, forming together the extracellular bone matrix (ultrastructure). A Mori–Tanaka scheme relates the stiffnesses and volume fractions of the extrafibrillar space and the fibril to the homogenized elasticity tensor of the extracellular bone matrix [specification of (5.10) for RVE of Fig. 5.4d]. The fifth homogenization step refers to an observation scale of about 100 μm, where lacunar pores are embedded in an ultrastructural matrix building up the extravascular bone material. A Mori–Tanaka scheme relates the stiffnesses and volume fractions of the ultrastructure and the lacunae to the homogenized elasticity tensor of the extravascular bone material [specification of (5.10) for RVE of Fig. 5.4e]. The sixth homogenization step refers to an observation scale of about 1 mm, where the extravascular matrix is perforated by Haversian canals, building up the microstructure. A Mori–Tanaka scheme relates the stiffnesses and volume fractions of the extravascular bone material and the Haversian canals to the homogenized elasticity tensor of the microstructure [specification of (5.10) for RVE of Fig. 5.4f].

In addition, repeated specification of (5.6) for all RVEs in Fig. 5.4 allows for upscaling strains from the level of the elementary components, all the way up to the macroscopic bone material of Fig. 5.4f. Considering, in addition, the elastoplastic behavior of sliding hydroxyapatite minerals [11, 42], according to (5.11), (5.1), and (5.2), the elastoplastic material behavior at all scales is defined, inclusive of quasi-brittle failure once the collagen failure surface, (5.12), is reached.

5.6 Experimental Validation of Multiscale Micromechanics Theory for Bone

The micromechanical model of Sect. 5.5 predicts, for each set of tissue-specific volume fractions, the corresponding tissue-specific elasticity and strength properties at all observation scales of Fig. 5.4. Thus, a strict experimental validation of this

model is realized as follows: (1) different sets of *volume fractions* [variables f_r in (5.1)–(5.10)] are determined from composition experiments on different bone samples with different ages, from different species and different anatomical locations; (2) these volume fractions are used as model input, and (3) corresponding model-predicted *stiffness and strength values* [model output, (5.10)] are compared to results from stiffness and strength experiments on the same or very similar bone samples.

The *volume fractions* within each of the considered RVEs (Fig. 5.4) are accessible through the following experiments: At the microstructural and the extravascular observation scales (Fig. 5.4e,f), polarized light microscopy (Fig. 5.2f) visualizes, in cortical bone, Haversian canals and lacunae [27, 43, 44], from which the vascular and lacunar porosities can be derived, see [41] for details. For determination of the volume fractions in all other RVEs, the pioneering volume measurements and weighing experiments on wet, dehydrated, and demineralized cortical bone specimens, performed by Lees [16, 45, 46], are of central importance; they give access to the mineral, (molecular) collagen, and water content at the extracellular scale (Fig. 5.2d and RVE Fig. 5.4d). The collagen volume fraction in a piece of extracellular bone material (Fig. 5.2d and Fig. 5.4d), together with the spatial organization of collagen molecules within the extracellular matrix, characterized by a staggered longitudinal arrangement quantified by the Hodge–Petruska scheme [47] and by a quasi-hexagonal transverse arrangement as elucidated by the pioneering neutron diffraction experiments of Lees and coworkers [16, 37], gives access to the volume fraction of collagen fibrils in an extracellular RVE (Fig. 5.4d, see [41] for details). Concerning the RVEs below the extracellular scale (Fig. 5.4b,c), their mineral volume fraction can be determined from Hellmich and Ulm's finding [48] that the hydroxyapatite concentration in the extra-collagenous space is the same inside and outside the fibrils, see [41] for details. The class of porous hydroxyapatite biomaterials [32, 33, 49–52] directly mimics the porous polycrystal of Fig. 5.4c. For such materials, referred to in Fig. 5.5a–d, the mineral volume fraction is directly related to porosity or apparent mass density, accessible from mass and volume measurements on biomaterial samples. Finally, the ultrastructural collagen volume and that of wet collagen in fibrils (Fig. 5.4b) give access to the intermolecular porosity within an RVE of wet collagen (see Fig. 5.4a and [41] for details).

Stiffness and strength values are gained from ultrasonics experiments on cortical [43–46, 53] and on trabecular bone samples [54], and from quasi-static uniaxial, compressive or tensile, mechanical tests [42, 55–71] (see [11, 34, 41] for details).

Throughout all different observation scales, and across a great variety of bone tissues (from different anatomical locations of different mammals including humans, cows, elephants, deers, rabbits, and horses), micromechanics model predictions for stiffness and strength agree very well with corresponding experimental data (see Fig. 5.5). This unparalleled quantification of bone's mechanical behavior allows us to draw basic conclusions on how bone works mechanically – described in the next chapter.

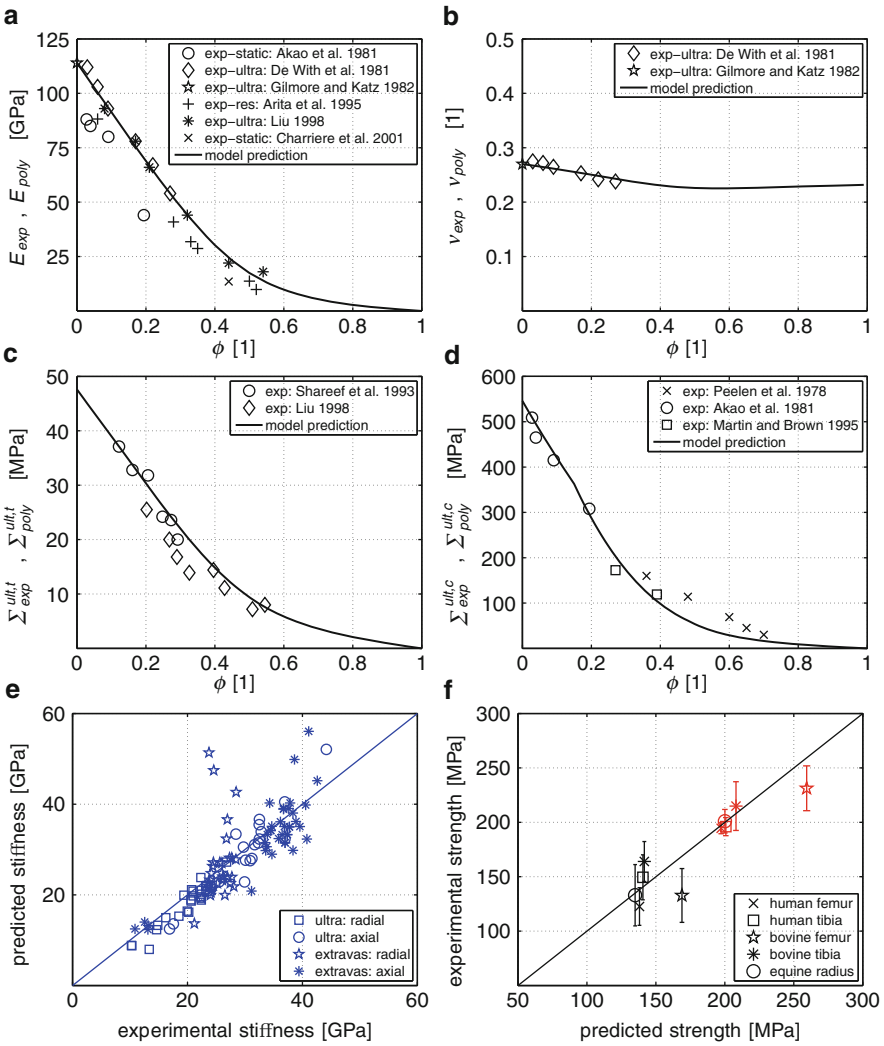

Fig. 5.5 Comparison between micromechanical model predictions and corresponding experiments: (**a, b**) elasticity in terms of Young's modulus E and Poisson's ratio ν of hydroxyapatite biomaterials (see Fig. 5.4c, [34]); (**c, d**) uniaxial tensile and compressive strength of hydroxyapatite biomaterials (see Fig. 5.4c, [34]); (**e**) radial and axial normal stiffness (C_{1111} and C_{3333}) of cortical and trabecular bone at ultrastructural (ultra) and extravascular (exvas) scales (see Fig. 5.4d,e, [41]); (**f**) uniaxial strength of cortical bone at the macroscopic scale (see Fig. 5.4f, [11]), with mean and standard deviation being depicted for experimental tensile strength (*dark color*) and experimental compressive strength (*light color*)

5.7 How Bone Works: Mechanical Design Characteristics of Bone Revealed Through Multiscale Micromechanics

Bone materials are built up in a remarkably anisotropic fashion, with respect to both stiffness and strength.

As regards elasticity, the experimentally verified micromechanics theory of Sects. 5.5 and 5.6 reveals the following sources of anisotropy:

1. The intrinsic anisotropy of molecular collagen, quantified through Brillouin light scattering tests of Cusack and Miller [17] and given at the bottom of Table 5.1;
2. The axially oriented arrangement of molecular collagen in the mineralized collagen fibril (Fig. 5.4b); of the mineralized collagen fibrils in the extracellular bone matrix (Fig. 5.4d); and of the vascular porosity (Haversian canals) in cortical bone (Fig. 5.4f).

In contrast, bone mineral is poorly organized [20, 24, 72–75], so that bone materials without collagen and vascular pores, such as hyperpycnotic tissues [16,76] or artificial hydroxyapatite biomaterials [29,32,51,52,77,78], represented basically through the extrafibrillar RVE of Fig. 5.4c, are virtually isotropic. At the same time, the high connectivity of the individual crystals, forming a porous polycrystal in the extrafibrillar space of bone materials, is important for providing sufficient transverse stiffness.

As regards strength, the micromechanics model of Sects. 5.5 and 5.6 shows an additional feature beyond anisotropy, namely the sensitivity of bone to tensile versus compressive loading type (not existing in the elastic regime): The extrafibrillar space (see Fig. 5.2c and RVE in Fig. 5.4c) is ten times weaker under tensile loading than under compressive loading, a characteristic which it shares with a lot of other quasi-brittle materials, such as sandstone or concrete [79]. The reason for that lies in the localization or concentration of homogeneous tensile or compressive strains from the boundary of the extrafibrillar RVE into its individual needle phases, leading eventually to failure of the most unfavorably stressed needle according to criterion (5.11) (see Fig. 5.6). In overall uniaxial tension, this local failure is dominated by tensile normal stresses in needle phases more or less aligned with the loading direction (for more or less porous materials; see Fig. 5.6a,b). In overall uniaxial compression, however, the aforementioned local failure is still dominated by tensile normal stresses in one needle phase – this phase now being aligned more or less perpendicular to the loading direction (for more or less porous materials; see Fig. 5.6c,d). Accordingly, it takes much more overall compressive stresses to produce as much normal tensile stresses in needles perpendicular to the loading direction than tensile stresses in needles aligned with the loading direction, stemming from overall tensile loads. This explains the ratio of 1:10 between tensile and compressive strength in hydroxyapatite biomaterials.

In real bones, however, two differences with respect to this situation are significant:

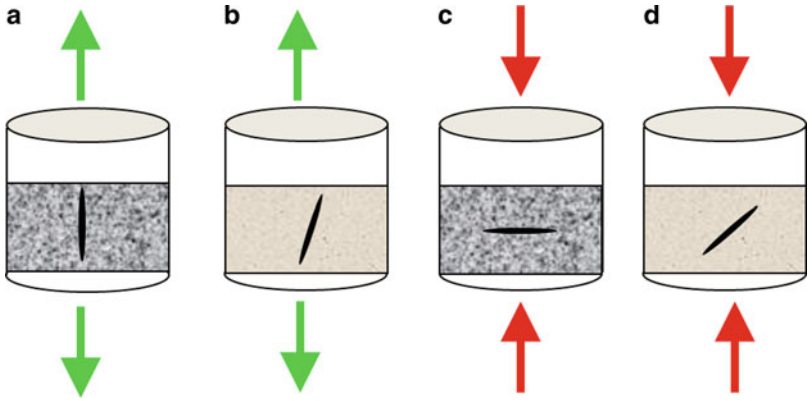

Fig. 5.6 Orientation of crystal needle initiating overall failure of hydroxyapatite polycrystals, under tensile (**a, b**) and compressive (**c, d**) uniaxial macroscopic loading: (**a, c**) local tensile failure in highly porous polycrystals; (**b, d**) local combined tensile-shear failure in polycrystals with low porosity

1. The hydroxyapatite crystals are nanometer-sized instead of micrometer-sized, so that they are intimately bond to the structured water layers between them [80–83]. This evokes ideal plastic sliding rather than brittle failure, once the elastic regime of the crystals is left.
2. Molecular collagen (shown to be quasi-brittle, both experimentally [36] and computationally [84]) reinforces the multiporous hierarchical nanocomposite "bone" both in axial tension and in axial compression, up to the same extent. Accordingly, bone materials show a tensile-to-compressive strength ratio of 2:3, instead of 1:10.

Bone replacement materials should mimic these "microstructural mechanics", features as closely as possible if an imitation of the natural form of bone is desired [105]. Hence, the design characteristics of natural bone imply the following design rules for creating bone replacement materials close to their natural "prototypes":

- Use of an anisotropic organic template
- Growth of nanometer-sized mineral crystals
- Realization of a connected network of crystals

In this context, the following recent developments in the bone biomaterials community seem noteworthy: As regards anisotropic organic templates, recent bone biomaterials rely on materials such as starch [85], chitosan [86], or collagen itself [87–92]. While micron-sized hydroxyapatite crystals defined the state of the art in biomaterial production in the 1980s and 1990s [32, 33, 50, 77], modern processing techniques, such as sol–gel combustion [93] or precipitation from an aqueous

solution [87,88,92,94–97], allow for production of nanometer-sized hydroxyapatite crystals. Finally, also interconnected networks of hydroxyapatite crystals could be recently produced, by means of a layer-by-layer deposition method [92].

5.8 Some Conclusions from a Biological Viewpoint

To the knowledge of the authors, the aforementioned design rules concern all different kinds of bones, across the entire subphylum *vertebrata*, in the sense that they satisfactorily explain, in a unified fashion, the large variety of mechanical properties depicted in Fig. 5.5e,f. In this sense, they are "universal" for the vertebrates, but not beyond this subphylum. The aforementioned design principles may result from "architectural constraints" [98, 99] merely due to once chosen material constituents and their physical interactions that imply the fundamental hierarchical organization patterns or basic building plans of bone materials (see Fig. 5.2), which remain largely unchanged during biological evolution. In this sense, it seems highly probable that the same principles hold for extinct species like dinosaurs, although this cannot be tested in full completeness, as fossils are chemically altered postmortem [100].

Mineralized skeletal structures built up of bone typically span three orders of magnitude (Fig. 5.7), whereby the mammals currently define the upper size limit. The concept of an inner skeleton ("endoskeleton") is also followed out of the phylum *chordata*, namely with sponges (using either silica or calcium carbonates as mineral, Fig. 5.7) and with phylum *echinodermata*, based on mineralized tissues containing calcium carbonates (Fig. 5.7). The same holds for certain members of phylum *mollusca*, namely cephalopods (Fig. 5.7). Alternatively, load-carrying organs may be realized as outer skeletons (exoskeletons), at tiny formats containing silica (e.g., in diatoms), and at larger formats containing calcium carbonates and chitin as organic component (with phylum *arthropoda* and with all classes of phylum *mollusca* except for certain cephalopods, see Fig. 5.7).

Elementary components	Skeleton	Taxon	Typical length (metres)						
			10^{-4}	10^{-3}	10^{-2}	10^{-1}	10^{0}	10^{1}	10^{2}
Hydroxyapatite, organics (mainly collagen), water - building up bone tissues	Endoskeleton	Osteichthyes			■	■	■		
		Amphibians			■	■	■		
		Reptiles			■	■	■	■	
		Birds			■	■	■		
		Mammals			■	■	■	■	■
Calcium carbonates, organics (including chitin), water	Exoskeleton	Arthropods		■	■	■			
	Exo/endoskeleton	Molluscs		■	■	■	■	■	
Calcium carbonates, organics, water	Endoskeleton	Echinoderms			■	■			
		Calcareous sponges			■	■	■		
Silica, organics, water	Exoskeleton	Diatoms	■	■					
	Endoskeleton	Glass sponges, demosponges			■	■	■		

Fig. 5.7 Overview over elementary components of mineralized tissues and size of inner and outer skeletons built thereof, across the animal kingdom (see also [101–104])

References

1. Ch. Hellmich, D. Katti, Mechanics of biological and bioinspired materials and structures. J. Eng. Mech ASCE **35**(5), 365–366 (2009)
2. R. Hill, Elastic properties of reinforced solids: some theoretical principles. J. Mech. Phys. Solids **11**, 357–362 (1963)
3. P. Suquet, Effective behavior of nonlinear composites, in *Continuum Micromechanics*, ed. by P. Suquet (Springer, Wien, New York, 1997), pp. 197 – 264
4. A. Zaoui, Structural morphology and constitutive behavior of microheterogeneous materials, in *Continuum Micromechanics*, ed. by P. Suquet (Springer, Wien, New York, 1997), pp. 291–347
5. A. Zaoui, Continuum micromechanics: survey. J. Eng. Mech ASCE **128**(8), 808–816 (2002)
6. L. Dormieux, D. Kondo, F.-J. Ulm, *Microporomechanics* (Wiley, 2006)
7. R. Hill, Continuum micro-mechanics of elastoplastic polycrystals. J. Mech. Phys. Solids **13**, 89–101 (1965)
8. G.J. Dvorak, Transformation field analysis of inelastic composite materials. Proc. R. Soc. Lond. A **437**, 311–327 (1992)
9. J.D. Eshelby, The determination of the elastic field of an ellipsoidal inclusion, and related problems. Proc. R. Soc. Lond. A **241**, 376–396 (1957)
10. N. Laws, The determination of stress and strain concentrations at an ellipsoidal inclusion in an anisotropic material. J. Elasticity **7**(1), 91–97 (1977)
11. A. Fritsch, Ch. Hellmich, L. Dormieux, Ductile sliding between mineral crystals followed by rupture of collagen crosslinks: experimentally supported micromechanical explanation of bone strength. J. Theor. Biol. **260**, 230–252 (2009)
12. T. Mori, K. Tanaka, Average stress in matrix and average elastic energy of materials with misfitting inclusions. Acta Metallurgica **21**(5), 571–574 (1973)
13. K. Wakashima, H. Tsukamoto, Mean-field micromechanics model and its application to the analysis of thermomechanical behaviour of composite materials. Mater. Sci. Eng. A **146**(1–2), 291–316 (1991)
14. A.V. Hershey, The elasticity of an isotropic aggregate of anisotropic cubic crystals. J. Appl. Mech. ASME **21**, 236–240 (1954)
15. J.L. Katz, H.S. Yoon, S. Lipson, R Maharidge, A. Meunier, P. Christel, The effects of remodelling on the elastic properties of bone. Calcif. Tissue Int **36**, S31–S36 (1984)
16. S. Lees, Considerations regarding the structure of the mammalian mineralized osteoid from viewpoint of the generalized packing model. Connect. Tissue Res. **16**, 281–303 (1987)
17. S. Cusack, A. Miller, Determination of the elastic constants of collagen by Brillouin light scattering. J. Mol. Biol. **135**, 39–51 (1979)
18. A. Miller, Collagen: the organic matrix of bone. Philos Trans. R. Soc. Lond. B **304**, 455–477 (1984)
19. S. Lees, N.-J. Tao, M. Lindsay, Studies of compact hard tissues and collagen by means of Brillouin light scattering. Connect. Tissue Res. **24**, 187–205 (1990)
20. S. Lees, K.S. Prostak, V.K. Ingle, K. Kjoller, The loci of mineral in turkey leg tendon as seen by atomic force microscope and electron microscopy. *Calcif. Tissue Int.* **55**, 180–189 (1994)
21. S. Weiner, T. Arad, I. Sabanay, W. Traub, Rotated plywood structure of primary lamellar bone in the rat: orientation of the collagen fibril arrays. Bone **20**, 509–514 (1997)
22. S. Weiner, H.D. Wagner, The material bone: structure – mechanical function relations. Annu. Rev. Mater. Sci. **28**, 271–298 (1998)
23. J.-Y. Rho, L. Kuhn-Spearing, P. Zioupos, Mechanical properties and the hierarchical structure of bone. Med. Eng. Phys. **20**, 92–102 (1998)
24. K.S. Prostak, S. Lees, Visualization of crystal-matrix structure. In situ demineralization of mineralized turkey leg tendon and bone. Calcified Tissue Int. **59**, 474–479 (1996)
25. J.P.R.O. Orgel, T.C. Irving, A. Miller, T.J. Wess, Microfibrillar structure of type I collagen in situ. Proc. Natl. Acad. Sci. USA **103**(24), 9001–9005 (2006)

26. W.J. Landis, M.J. Song, A. Leith, L. McEwen, B.F. McEwen, Mineral and organic matrix interaction in normally calcifying tendon visualized in three dimensions by high-voltage electron microscopic tomography and graphic image reconstruction. J. Struct. Biol. **110**, 39–54 (1993)
27. S. Lees, P. Cleary, J.D. Heeley, E.L. Gariepy, Distribution of sonic plesio-velocity in a compact bone sample. J. Acoust. Soc. Am. **66**(3), 641–646 (1979)
28. J.L. Katz, K. Ukraincik, On the anisotropic elastic properties of hydroxyapatite. J. Biomech. **4**, 221–227 (1971)
29. R.S. Gilmore, J.L. Katz, Elastic properties of apatites. J. Mater. Sci. **17**, 1131–1141 (1982)
30. H. Yao, L. Ouyang, W.-Y. Ching, Ab initio calculation of elastic constants of ceramic crystals. J. Am. Ceramic Soc. **90**(10), 3194–3204 (2007)
31. W.Y. Ching, P. Rulis, A. Misra, Ab initio elastic properties and tensile strength of crystalline hydroxyapatite. Acta Biomater. **5**, 3067–3075 (2009)
32. M. Akao, H. Aoki, K. Kato, Mechanical properties of sintered hydroxyapatite for prosthetic applications. J. Mater. Sci. **16**, 809–812 (1981)
33. M.Y. Shareef, P.F. Messer, R. van Noort, Fabrication, characterization and fracture study of a machinable hydroxyapatite ceramic. Biomaterials **14**(1), 69–75 (1993)
34. A. Fritsch, L. Dormieux, Ch. Hellmich, J. Sanahuja, Mechanical behaviour of hydroxyapatite biomaterials: an experimentally validated micromechanical model for elasticity and strength. J. Biomed. Mater. Res. A **88A**, 149–161 (2009)
35. N. Bilaniuk, G.S.K. Wong, Speed of sound in pure water as a function of temperature. J. Acoust. Soc. Am. **93**(3), 1609–1612 (1993)
36. E. Gentleman, A.N. Lay, D.A. Dickerson, E.A. Nauman, G.A. Livesay, K.C. Dee. Mechanical characterization of collagen fibers and scaffolds for tissue engineering. Biomaterials **24**, 3805–3813 (2003)
37. S. Lees, L.C. Bonar, H.A. Mook, A study of dense mineralized tissue by neutron diffraction. Int. J. Biol. Macromol. **6**, 321–326 (1984)
38. Y.-L. Sun, Z.-P. Luo, A. Fertala, K.-N. An, Direct quantification of the flexibility of type I collagen monomer. Biochem. Biophys. Res. Commun. **295**, 382–386 (2002)
39. M.J. Buehler, Nanomechanics of collagen fibrils under varying cross-link densities: atomistic and continuum studies. J. Mech. Behav. Biomed. Mater. **1**, 59–67 (2008)
40. Ch. Hellmich, J.-F. Barthélémy, L. Dormieux, Mineral-collagen interactions in elasticity of bone ultrastructure – a continuum micromechanics approach. Eur. J. Mech. A Solids **23**, 783–810 (2004)
41. A. Fritsch, Ch. Hellmich, 'Universal' microstructural patterns in cortical and trabecular, extracellular and extravascular bone materials: micromechanics-based prediction of anisotropic elasticity. J. Theor. Biol. **244**(4), 597–620 (2007)
42. A.H. Burstein, J.J.M. Zika, K.G. Heiple, L. Klein, Contribution of collagen and mineral to the elastic-plastic properties of bone. J. Bone Joint Surg. **57A**, 956–961 (1975)
43. S. Lees, D. Hanson, E.A. Page, H.A. Mook, Comparison of dosage-dependent effects of beta-aminopropionitrile, sodium fluoride, and hydrocortisone on selected physical properties of cortical bone. J. Bone Miner. Res. **9**(9), 1377–1389 (1994)
44. R.N. McCarthy, L.B. Jeffcott, R.N. McCartney, Ultrasound speed in equine cortical bone: effects of orientation, density, porosity and temperature. J. Biomech. **23**(11), 1139–1143 (1990)
45. S. Lees, J.D. Heeley, P.F. Cleary, A study of some properties of a sample of bovine cortical bone using ultrasound. Calcif. Tissue Int. **29**, 107–117 (1979)
46. S. Lees, J.M. Ahern, M. Leonard, Parameters influencing the sonic velocity in compact calcified tissues of various species. J. Acoust. Soc. Am. **74**(1), 28–33 (1983)
47. A.J. Hodge, J.A. Petruska, Recent studies with the electron microscope on ordered aggregates of the tropocollagen molecule, in *Aspects of Protein Structure – Proceedings of a Symposium Held in Madras 14–18 January 1963 and Organized by the University of Madras, India*, ed. by G.N. Ramachandran (Academic, London, 1963), pp. 289–300

48. Ch. Hellmich, F.-J. Ulm, Average hydroxyapatite concentration is uniform in extracollagenous ultrastructure of mineralized tissue. Biomech. Model. Mechanobiol. **2**, 21–36 (2003)
49. J.G.J. Peelen, B.V. Rejda, K. de Groot, Preparation and properties of sintered hydroxylapatite. Ceramurgia Int. **4**(2), 71–74 (1978)
50. R.I. Martin, P.W. Brown, Mechanical properties of hydroxyapatite formed at physiological temperature. J. Mater. Sci. Mater. Med. **6**, 138–143 (1995)
51. D.-M. Liu, Preparation and characterisation of porous hydroxyapatite bioceramic via a slip-casting route. Ceramics Int. **24**, 441–446 (1998)
52. E. Charrière, S. Terrazzoni, C. Pittet, Ph. Mordasini, M. Dutoit, J. Lemaître, Ph. Zysset, Mechanical characterization of brushite and hydroxyapatite cements. Biomaterials **22**, 2937–2945 (2001)
53. R.B. Ashman, S.C. Cowin, W.C. van Buskirk, J.C. Rice, A continuous wave technique for the measurement of the elastic properties of cortical bone. J. Biomech. **17**(5), 349–361 (1984)
54. R.B. Ashman, J.Y. Rho, Elastic modulus of trabecular bone material. J. Biomech. **21**(3), 177–181 (1988)
55. J.D. Currey, Differences in the tensile strength of bone of different histological types. J. Anat. **93**, 87–95 (1959)
56. E.D. Sedlin, C. Hirsch, Factors affecting the determination of the physical properties of femoral cortical bone. Acta Orthop. Scand. **37**, 29–48 (1966)
57. A.H. Burstein, J.D. Currey, V.H. Frankel, D.T. Reilly, The ultimate properties of bone tissue: the effects of yielding. J. Biomech. **5**, 35–44 (1972)
58. D.T. Reilly, A.H. Burstein, The elastic modulus for bone. J. Biomech. **7**, 271–275 (1974)
59. D.T. Reilly, A.H. Burstein, The elastic and ultimate properties of compact bone tissue. J. Biomech. **8**, 393–405 (1975)
60. J.D. Currey, The effects of strain rate, reconstruction and mineral content on some mechanical properties of bovine bone. J. Biomech. **8**, 81–86 (1975)
61. A.H. Burstein, D.T. Reilly, M. Martens, Aging of bone tissue: mechanical properties. J. Bone Joint Surg. **58A**, 82–86 (1976)
62. R.P. Dickenson, W.C. Hutton, J.R. Stott, The mechanical properties of bone in osteoporosis. J. Bone Joint Surg. **63-B**(2), 233–238 (1981)
63. H. Cezayirlioglu, E. Bahniuk, D.T. Davy, K.G. Heiple, Anisotropic yield behavior of bone under combined axial force and tension. J. Biomech. **18**(1), 61–69 (1985)
64. R.B. Martin, J. Ishida, The relative effects of collagen fiber orientation, porosity, density, and mineralization on bone strength. J. Biomech. **22**, 419–426 (1989)
65. J.D. Currey, Physical characteristics affecting the tensile failure properties of compact bone. J. Biomech. **23**, 837–844 (1990)
66. R.W. McCalden, J.A. McGeough, M.B. Barker, C.M. Court-Brown, Age-related changes in the tensile properties of cortical bone. The relative importance of changes in porosity, mineralization, and microstructure. J. Bone Joint Surg. **75-A**(8), 1193–1205 (1993)
67. C.M. Riggs, L.C. Vaughan, G.P. Evans, L.E. Lanyon, A. Boyde, Mechanical implications of collagen fibre orientation in cortical bone of the equine radius. Anat. Embryol. **187**, 239–248 (1993)
68. S.C. Lee, B.S. Coan, M.L. Bouxsein, Tibial ultrasound velocity measured in situ predicts the material properties of tibial cortical bone. Bone **21**(1), 119–125 (1997)
69. S.P. Kotha, N. Guzelsu, Modeling the tensile mechanical behavior of bone along the longitudinal direction. J. Theor. Biol. **219**, 269–279 (2002)
70. J.D. Currey, Tensile yield in compact bone is determined by strain, post-yield behaviour by mineral content. J. Biomech. **37**, 549–556 (2004)
71. Ch. Hellmich, H.W. Müllner, Ch. Kohlhauser, Mechanical (triaxial) tests on biological materials and biomaterials. Technical Report DNRT3-1.2-3, Network of Excellence 'Knowledge-based Multicomponent Materials for Durable and Safe Performance – KMM-NoE', sponsored by the European Commission, October 2006
72. F. Peters, K. Schwarz, M. Epple, The structure of bone studied with synchrotron X-ray diffraction, X-ray absorption spectroscopy and thermal analysis. Thermochim. Acta **361**, 131–138 (2000)

73. M. Epple, Solid-state chemical methods to investigate the nature of calcified deposits. Zeitschrift für Kardiologie **90**(Suppl. 3), III/64–III/67 (2001)
74. V. Benezra Rosen, L.W. Hobbs, M. Spector, The ultrastructure of anorganic bovine bone and selected synthetic hydroxyapatites used as bone graft substitute material. Biomaterials **23**, 921–928 (2002)
75. Ch. Hellmich, F.-J. Ulm, Are mineralized tissues open crystal foams reinforced by crosslinked collagen? Some energy arguments. J. Biomech. **35**, 1199–1212 (2002)
76. S. Lees, D. Hanson, E.A. Page, Some acoustical properties of the otic bones of a fin whale. J. Acoust. Soc. Am. **99**(4), 2421–2427 (1995)
77. G. De With, H.J.A. van Dijk, N. Hattu, K. Prijs, Preparation, microstructure and mechanical properties of dense polycrystalline hydroxy apatite. J. Mater. Sci. **16**, 1592–1598 (1981)
78. I.H. Arita, D.S. Wilkinson, M.A. Mondragón, V.M. Castaño, Chemistry and sintering behaviour of thin hydroxyapatite ceramics with controlled porosity. Biomaterials **16**, 403–408 (1995)
79. H. Kupfer, H.K. Hilsdorf, H. Rusch, Behavior of concrete under biaxial stresses. ACI J. **66**, 656–666 (1969)
80. D. Zahn, O. Hochrein, Computational study of interfaces between hydroxyapatite and water. Phys. Chem. Chem. Phys. **5**, 4004–4007 (2003)
81. D. Zahn, O. Hochrein, A. Kawska, J. Brickmann, R. Kniep, Towards an atomistic understanding of apatite-collagen biomaterials: linking molecular simulation studies of complex-, crystal- and composite-formation to experimental findings. J. Mater. Sci. **42**, 8966–8973 (2007)
82. R. Bhowmik, K.S. Katti, D.R. Katti, Mechanics of molecular collagen is influenced by hydroxyapatite in natural bone. J. Mater. Sci. **42**, 8795–8803 (2007)
83. R. Bhowmik, K.S. Katti, D.R. Katti, Mechanisms of load-deformation behavior of molecular collagen in hydroxyapatite-tropocollagen molecular system: steered molecular dynamics study. J. Eng. Mech. **135**(5), 413–421 (2009)
84. M.J. Buehler, Nature designs tough collagen: explaining the nanostructure of collagen fibrils. Proc. Natl. Acad. Sci. USA **103**(33), 12285–12290 (2006)
85. J.F. Mano, C.M. Vaz, S.C. Mendes, R.L. Reis, A.M. Cunha, Dynamic mechanical properties of hydroxyapatite-reinforced and porous starch-based degradable biomaterials. J. Mater. Sci. Mater. Med. **10**, 857–862 (1999)
86. D. Verma, K. Katti, D. Katti, Effect of biopolymers on structure of hydroxyapatite and interfacial interactions in biomimetically synthesized hydroxyapatite/biopolymer nanocomposites. Ann. Biomed. Eng. **36**(6), 1024–1032 (2008)
87. C. Du, F.Z. Cui, X.D. Zhu, K. de Groot, Three-dimensional nano-HAp/collagen matrix loading with osteogenic cells in organ culture. J. Biomed. Mater. Res. A **44**(4), 407–415 (2004)
88. J.D. Hartgerink, E. Beniash, S.I. Stupp, Self-assembly and mineralization of peptide-amphiphile nanofibers. Science **294**, 1684–1688 (2001)
89. D.A. Wahl, J.T. Czernuszka, Collagen-hydroxyapatite composites for hard tissue repair. Eur. Cells Mater. **11**, 43–56 (2006)
90. S.A. Catledge, W.C. Clem, N. Shrikishen, S. Chowdhury, A.V. Stanishevsky, M. Koopman, Y.K. Vohra, An electrospun triphasic nanofibrous scaffold for bone tissue engineering. Biomed. Mater. **2**(2), 142–150 (2007)
91. D.W. Green, Tissue bionics: examples in biomimetic tissue engineering. Biomed. Mater. **3**, 034010 (2008)
92. A. Ficai, E. Andronescu, G. Voicu, D. Manzu, M. Ficai, Layer by layer deposition of hydroxyapatite onto the collagen matrix. Mater. Sci. Eng. C **29**, 2217–2220 (2009)
93. Y. Han, S. Li, X. Wang, X. Chen, Synthesis and sintering of nanocrystalline hydroxyapatite powders by citric acid sol–gel combustion method. Mater. Res. Bull. **39**, 25–32 (2004)
94. A. Tampieri, G. Celotti, El. Landi, M. Sandri, N. Roveri, G. Falini, Biologically inspired synthesis of bone-like composite: self-assembled collagen fibers/hydroxyapatite nanocrystals. J. Biomed. Mater. Res. A, **67A**(2), 618–625 (2003)

95. Ch. Jäger, T. Welzel, W. Meyer-Zaika, M. Epple, A solid-state NMR investigation of the structure of nanocrystalline hydroxyapatite. Magn. Reson. Chem. **44**(6), 573–580 (2006)
96. G.E. Poinern, R.K. Brundavanam, N. Mondinos, Z.-T. Jiang, Synthesis and characterisation of nanohydroxyapatite using an ultrasound assisted method. Ultrason. Sonochem. **16**, 469–474 (2009)
97. R. Khanna, K.S. Katti, D.R. Katti, Nanomechanics of surface modified nanohydroxyapatite particulates used in biomaterials. J. Eng. Mech ASCE **135**(5), 468–478 (2009)
98. A. Seilacher, Arbeitskonzept zur Konstruktionsmorphologie (Concept for structure-morphology). Lethaia **3**, 393–396 (1970), in German
99. S.J. Gould, R.C. Lewontin, The spandrels of San Marco and the Panglossian paradigm: a critique of the adaptionist program. Proc. R. Soc. Lond. B **205**(1161), 581–598 (1979)
100. Y. Kolodny, B. Luz, M. Sander, W.A. Clemens, Dinosaur bones: fossils or pseudomorphs? the pitfalls of physiology reconstruction from apatitic fossils. Palaeogeogr. Palaeoclimatol. Palaeoecol. **126**, 161–71 (1996)
101. N.K. Mathur, C.K. Narang, Chitin and chitosan, versatile polysaccharides from marine animals. J. Chem. Educ. **67**, 938–942 (1990)
102. S. Weiner, L. Addadi, H.D. Wagner, Materials design in biology. Mater. Sci. Eng. C **11**, 1–8 (2000)
103. S. Lees, Elastic properties and measurement techniques of hard tissues, in *Handbook of Elastic Properties of Solids, Liquids, and Gases*, Volume III: Elastic Properties of Solids, Chapter 7, ed. by M. Levy, H. Bass, R. Stern (Academic, New York, 2001), pp. 147–181
104. H.C.W. Skinner, A.H. Jahren, Biomineralization, in *Treatise on Geochemistry*, Volume 8: Biogeochemistry, Chapter 4, ed. by W.H. Schlesinger (Elsevier, Amsterdam, The Netherlands, 2003), pp. 117–184
105. I.C. Gebeshuber, H. Stachelberger, B.A. Ganji, D.C. Fu, J. Yunas, B.Y. Majlis, Exploring the innovational potential of biomimetics for novel 3D MEMS. Adv. Mater. Res. **74**, 265–268 (2009)